Article

Holistic Electric Powertrain Component Design for Battery Electric Vehicles in an Early Development Phase

Nico Rosenberger, Silvan Deininger, Jan Koloch and Markus Lienkamp

Article

Holistic Electric Powertrain Component Design for Battery Electric Vehicles in an Early Development Phase

Nico Rosenberger *, Silvan Deininger, Jan Koloch and Markus Lienkamp

Institute of Automotive Technology, Department of Mobility Systems Engineering, TUM School of Engineering & Design, Technical University of Munich, Boltzmannstr. 15, 85748 Garching, Germany
* Correspondence: nico.rosenberger@tum.de; Tel.: +49-89-289-15906

Abstract: As battery electric vehicles (BEVs) gain significance in the automotive industry, manufacturers must diversify their vehicle portfolios with a wide range of electric vehicle models. Electric powertrains must be designed to meet the unique requirements and boundary conditions of different vehicle concepts to provide satisfying solutions for their customers. During the early development phases, it is crucial to establish an initial powertrain component design that allows the respective divisions to develop their components independently and minimize interdependencies, avoiding time- and cost-intensive iterations. This study presents a holistic electric powertrain component design model, including the high-voltage battery, power electronics, electric machine, and transmission, which is meant to be used as a foundation for further development. This model's simulation results and performance characteristics are validated against a reference vehicle, which was torn down and tested on a vehicle dynamometer. This tool is applicable for an optimization approach, focusing on achieving optimal energy consumption, which is crucial for the design of battery electric vehicles.

Keywords: battery electric vehicles; electric powertrain component design

1. Introduction

The 21st century has ushered in an era of unprecedented environmental challenges and growing concerns for environmental protection and energy conservation [1]. Especially the transportation sector has received heavy criticism due to excessive consumption of fossil fuels and resultant greenhouse gas (GHG) emissions. These GHGs possess a self-reinforcing global warming potential (GWP) [2]. Of particular concern are passenger cars, which account for approximately two-thirds of total road emissions in the European Union (EU) [3].

One recent decision by the European Parliament aims to reduce all CO_2 emissions by 55 % until 2030, including those from the automotive sector [4]. Furthermore, there are discussions of potentially banning internal combustion engine vehicles (ICEVs) from sales starting in 2035 [4] to accomplish emission-free urban passenger transport by 2050 [3].

Consequently, the automotive industry must swiftly adapt by replacing ICEVs with emission-free solutions. Currently, the most promising alternative is BEVs, which are locally emission-free and have demonstrated significant potential in recent years [5].

Ultimately, the final purchase decision rests with the customer. BEVs offer numerous advantages compared with traditional ICEVs, such as noise optimization, increased functional comfort, and high acceleration [6]. Nevertheless, the most crucial performance indicators for consumers besides the design are purchase cost and total cost of ownership, and particularly for BEVs, their electric range [7–9].

Subsequently, this study focuses on optimizing the electric range and energy consumption during the design of electric powertrain components. These values are primarily determined in the early development phase. Therefore, we present a holistic simulation framework for BEVs. Starting to optimize the electric powertrain component design holistically so early in the development process offers several advantages:

First, efficiency can be increased by optimizing the complete powertrain instead of focusing on individual components. This approach emphasizes the interaction between components, resulting in the detection of a holistic optimal efficiency. This improves energy utilization and increases electric range [10]. Second, holistic optimization aids in properly sizing the powertrain components. Since the complete powertrain is considered comprehensively, oversizing or undersizing individual components is prevented. This improves overall performance and reduces weight and costs [11,12]. Third, during the early stages of development, modifications to the powertrain layout do not cause significant issues. Therefore, it is crucial to demonstrate a fully operational and compatible powertrain concept. In contrast, changes in later stages can be exceedingly costly due to the precise calibration of the components to match their intended use. Even minor mass or volume changes provoke a domino effect of modifications in all other modules to conform to the new requirements. This phenomenon is known as the secondary mass effect in the automotive industry [10].

In the literature, multiple studies focus on specific components of electric powertrains, such as the high-voltage battery, according to the UN ECE R100 standard [13]. These studies all present methodologies and concepts for modeling high-voltage batteries, either using analytical or white box models [14–17], semi-empirical or grey box models [18–22], or fully relying on neural networks or black box models [23,24].

Similarly, studies on power electronics mostly rely on comparisons between insulated-gate bipolar transistors (IGBTs) and metal-oxide-semiconductor field-effect transistors (MOSFETS) [25–27] or different control strategies [28–30]. They present concepts on the design and its application for specific vehicles and respective electric machines [31–33]. Also, efficiency optimization strategies based on thermal management and power losses are investigated [34–37].

Closely connected to the concepts of power electronics, many studies focus on electric machines. Hereby, the focus lies mostly on designing flux-optimal concepts [38–40] or concepts with low friction losses [41–44], allowing for high-speed solutions by considering power and thermal losses [45,46]. Optimization strategies rely on drive cycle efficiency [47] or even multi-criteria evaluation, such as optimal rotor concepts [48–50].

Transmission studies in comparison either focus on single optimization features like mass and volume [51], gear ratio optimizations [52], or focus on multi-criteria optimization goals like incorporating the most efficient gearbox model in a given installation space [53–56]. To find such optimal solutions, studies investigated different transmission topologies [57,58], cooling concepts [59], lubricants [60], and single- or multi-speed transmission designs [61,62].

Some of the presented works consider the components under study with the directly connected components or the installation of different designs in a vehicle and evaluate their impact on the vehicle level. Nonetheless, none of these studies evaluate their respective component in combination with the remaining powertrain components.

1.1. Contributions

Therefore, in this study, we present a holistic electric powertrain component design methodology to apply in an early development phase. The resulting powertrain consists of harmonized components presenting a holistically optimal solution for a specific vehicle concept, which supports the respective design divisions, avoiding major design changes

and, thus, interdependencies between the components. To achieve meaningful results, we apply the current state-of-the-art's most promising detailed numerical simulation tools for the respective component and collocate the results in a simulation framework. We prove our concept and the quality of our simulation by evaluating our model against real vehicle data [63]. In this simulation framework, single-parameter configurations can be evaluated. Still, ultimately, the scope of this model is an optimization approach to identify the optimal parameter configuration regarding a targeted vehicle concept. Since the applied numerical simulation tools require high computational effort, we present optimization methods to improve the simulation time by neglecting less expedient configurations.

1.2. Layout

The structure of this article is divided into four sections. In Section 2, we start with the overall simulation framework and explain its architecture before explaining the models for the respective powertrain components in detail. After the simulation tool is presented, in Section 3, we validate our simulation tool by manually setting the design parameters to represent a real vehicle that was torn down and assessed on a vehicle dynamometer and compare their results. After validating the tool, we apply our optimization approach and show its functionality for a test vehicle concept. Before summarizing our methodology and its results in Section 4, we show optimization strategies that neglect less effective parameter configurations, applying pre-evaluations to improve computation time.

2. Methodology

In this section, we explain the structure of our methodology. Starting with the overall simulation framework, we describe the chronological process within our simulation concept before taking a detailed look into the respective component models.

2.1. Simulation Framework Concept

The main objectives of the framework are holism and modularity, and its structure is designed for optimization purposes. Combining a wide range of simulation tools within the respective component modules to achieve promising results and incorporating these into one unified framework, we secure holistic results. The modularity of the component models offers changes in the level of detail and so switches the focus of the investigation to specific components. Figure 1 shows the simulation framework in detail.

As shown in the figure, the components are designed in different simulation programs, which are discussed within the respective sections. The main program incorporating the results from the additional software programs, or rather the *optimization framework*, is implemented in *Matlab/Simulink* from *The Mathworks Inc., Natick, MA, USA* [64].

Starting the framework, the *vehicle requirements* need to be defined to design a powertrain for a specific vehicle concept, such as its electric range, its acceleration time from standstill to 100 $\frac{km}{h}$, and its top speed, which are key attributes for customers [9]. In Table A1 in Appendix A, all vehicle requirements are listed. In combination with constant parameters from literature recommendations [57,65–68], shown in Tables A3 and A4 in Appendix B, all necessary parameters for the *pre-initialization* step are given. Within this module, a vehicle model is built, and the framework is adapted to the chosen conditions, which will be explained in the respective component sections.
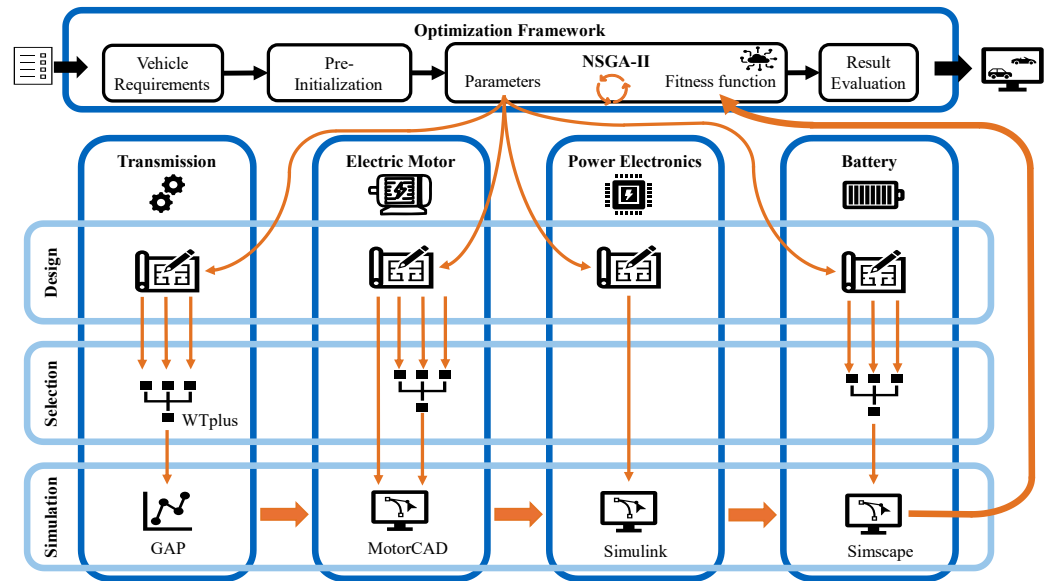
Figure 1. Simulation framework of the electric powertrain component design process.

In the *NSGA-II* module, the optimization algorithm is integrated. As the name indicates, this optimization method is based on the Nondominated Sorting Genetic Algorithm (NSGA)-II described in [69]. This algorithm represents the common choice in such analyses [70–72] and, therefore, is chosen for its ability to simultaneously optimize multiple objectives. All design parameters, concatenated in Table A5 in Appendix B, are fed from the NSGA-II module to the respective component modules and vary within their boundaries. For a chosen parameter configuration, the vehicle model is updated, and parameters are transferred to the transmission module, where outputs build the inputs for the following component module. Unlike the power flow from the high-voltage battery through the electric machine to the vehicle's wheels, we perform a backward simulation, where the given requirements from the wheels are delivered to the transmission and, thus, finally, to the high-voltage battery to determine power demands. From the battery back to the NSGA-II module, the results are fed into the fitness function. Within this function, powertrain parameters like its mass and volume, representing the results from the respective component modules, and vehicle performance parameters such as energy consumption and maximum acceleration, which are determined in performance tests on a vehicle level based on the component results, are concatenated and evaluated in the *result evaluation* applying the *gamultiobj* function in Matlab, emerging in a Pareto front based on the defined weighting factors. The evaluation parameters for the presented study are collected in Table A2 in Appendix A, consisting of cumulated component results and vehicle results based on the component characteristics. The results on the vehicle level are computed through an acceleration run determining the maximum speed and acceleration of the vehicle and an energy consumption simulation applying a predefined drive cycle determining the total energy consumption.

In the acceleration test, the vehicle performance is evaluated and compared with the vehicle's capacity to reach the desired acceleration time from 0–100 $\frac{km}{h}$ and the desired top speed. If the performance targets are not achieved, the simulation is stopped, and the parameter configuration is aborted. The main factors limiting the acceleration for BEVs are the maximum torque of the electric machine and the maximum power of the high-voltage battery, according to multiple recent studies [73–75].

In the first part of the acceleration test, the available torque is the limiting factor of the maximum acceleration until the maximum power of one of the components is reached, which limits the maximum acceleration. Based on the method proposed by Donoghue

et al. [73], a constant acceleration is initially implemented to assess the time required to reach 100 $\frac{km}{h}$. After that, the velocity profile transitions to a constant power state, with approximately 50% of the vehicle's acceleration capacity, which is implemented since the time to reach the top speed of the vehicle is not a fixed design goal and therefore prevents the vehicle's components from running in short-term overload, which is not activated during the second part of the acceleration cycle.

The second performance test is a drive cycle test intending to investigate the vehicle concept's energy consumption and, most importantly for BEVs, its range [9]. In this study, the Worldwide Harmonized Light Vehicles Test Procedure (WLTP) is applied, which is the European standard for evaluating BEVs's energy consumption and electric range [76], whereas the framework also allows for individual drive cycles.

2.2. Component Design

Independent of a potential optimization approach, the electric powertrain design starts with a parameter configuration and performs a backward simulation. During an optimization approach, every design parameter configuration, called an individual in evolutionary algorithms, in the population updates the vehicle model within its boundaries. It feeds information, such as wheel demands to meet the performance requirements, to the first component, the transmission. The transmission design transfers these wheel demands, such as torques and speeds, into shaft demands of the electric machine, which is designed accordingly. Within the electric machine, the mechanical demands are converted into electrical demands, which are then converted from alternating current (AC) into direct current (DC) demands within the power electronics module. These are finally processed within the high-voltage battery design section into vehicle power demands and, thus, into the input parameters for the two performance tests.

2.2.1. Transmission

The first component within the powertrain design is the transmission. For a given configuration of design parameters in Table A5 and the mechanical demands of the respective vehicle model, the transmission design is initiated. These parameters have been chosen since they directly influence the overall efficiency and, thus, power losses. The boundary conditions for these parameters have been set to cover the current state-of-the-art in BEVs. In addition to the design parameters, which are varied within the optimization module, parameters such as the gear width of both stages and the final topology are optimized within this module. In the first step, further transmission parameters are calculated following target-oriented design strategies, such as smaller modules for the first gear since less torque is applied. The simulation software applied in this module is *WTplus* [59,77].

With the necessary gear characteristics calculated, the transmission design starts. The high torque from a standstill allows electric vehicles to accelerate sufficiently fast with a single-speed architecture. Single-speed transmissions also reduce the transmission weight significantly and have lower mechanical losses compared with traditional transmissions [78]. Therefore, in this study, we focus on the four most common single-speed transmission topologies, which are shown in Figure 2. The topologies can be further divided into parallel axles concepts, such as topology 1 and 3, and coaxial transmissions, such as topologies 2 and 4.
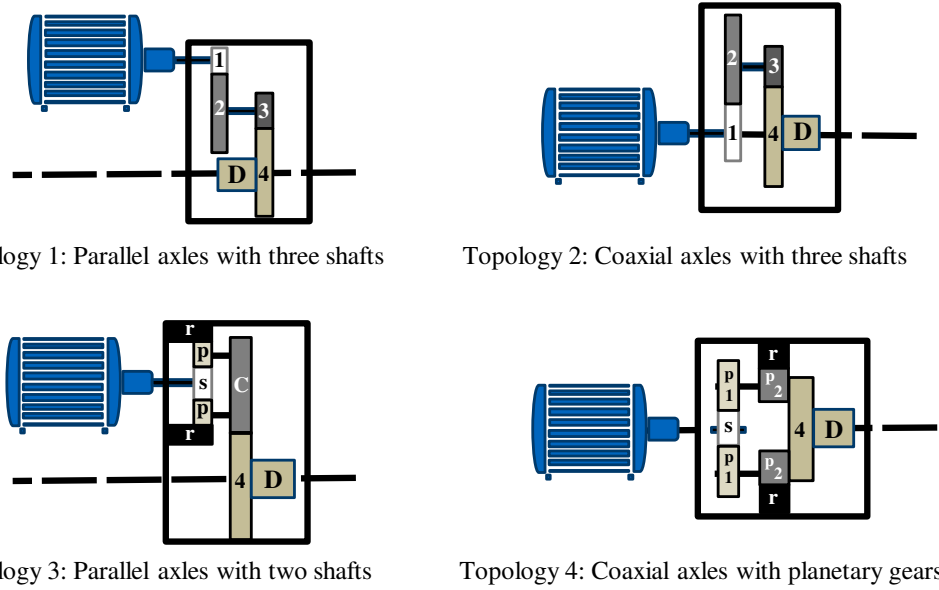
Topology 1: Parallel axles with three shafts

Topology 2: Coaxial axles with three shafts

Topology 3: Parallel axles with two shafts

Topology 4: Coaxial axles with planetary gearsets

Figure 2. The four most common single-speed transmission topologies [51]. The numbers reference the shaft number, and the letters represent the differential (D), sun gear (s), planet gears (p), and the ring gear (r).

Topology 1 contains two helical gear sets with independent axles. It is the most common layout due to the lowest complexity, as the two stages are independent with a distinct axis. The given parameters directly allow for the computation of the center radius and pitch circle center of each stage. Topology 2 is similar to the first one except for the center distances, which must be the same for the two gear sets due to the coaxial layout. Therefore, the motor output shaft needs to be hollow in order to accommodate the transmission output shaft. This leads to a compact design but also increases complexity. The second stage is calculated first in order to determine the center distance. In topology 3, a planetary gear set is used in the first stage; no pinion gear but a set of one sun gear (s), three planetary gears (p), and a ring gear (r) with a planet carrier are applied. In this case, the ring gear is stationary to the gearbox housing, and the planet carrier serves as the output of the first stage. Combining a helical gear set with a planetary one increases the transmission ratio of the first stage compared with conventional gears. This leads to a smaller transmission ratio for the second stage, effectively reducing its radial dimension. For the planetary stage, the calculations differ from the ones for the first two topologies. The sum of the number of teeth for the sun and planet gears needs to be divided by the number of planets. It is also crucial to maintain coaxiality between the sun and ring gear. Finally, the number of teeth also has to fulfill the following inequality [79]:

$$z_p < \frac{z_s + z_r}{2},$$

(1)

where z_p yields the tooth number of planetary gears, z_s the number of the sun gear tooth, and z_r the ring gear tooth number.

Topology 4 is the most compact but also the most complex version due to two linked planetary gear sets. The two-stage planetary gear set needs to be designed collectively. Therefore, a gear ratio for the first stage is eliminated in this topology. Like topology 3, the number of teeth in the first stage accounts for the sun gear, and stage two represents the small planetary gear. This topology needs to meet assembly and coaxial conditions, which result in the following equation:

$$\frac{z_{s1=s} \cdot z_{p2} + z_{p1} \cdot z_{r2=r}}{n_p \cdot \delta} \in \mathbb{Z},$$

(2)

with n_p being the number of planets and δ being the largest total divisor of the planet tooth number [79].

After the gear dimensions of all topologies are defined, the shaft dimensions can be determined. For shafts subjected to torque and bending, the minimum required diameter is calculated analytically for normal and hollow shafts, respectively [80]. If both loads are combined, equivalent bending moments M_{eq} are concatenated in

$$M_{eq} = \sqrt{M_B^2 + \frac{3}{4} \cdot M_T^2},$$ (3)

where M_B describes the moments caused by bending and M_T moments caused by torsion, and incorporated in the calculations to determine the minimum diameter for the shafts [81]. Bearings are selected from the rolling bearings catalog from *AB SKF, Gothenburg, Sweden* [82]. Whereas we selected deep groove bearings for spur gear sets and needle roller bearings for the planetary gear sets, the focus was to select general bearings for general validity. According to the shaft diameter, the respective bearing from the high-speed range is selected.

Before the transmission design is completed, a safety check is performed in the *STplus* software module connected to WTplus, representing a transmission design software calculating parameters such as efficiencies and temperature distributions [59,77]. To prevent premature failure, safety factors for the two main mechanisms of failure are introduced: S_H for surface pitting and S_F for tooth root breakage [83]. If these factors are sufficient, the gears will have enough load capacity for the application. If not, the gear width will be increased, according to Hofstetter et al. [55], to meet the predefined safety requirements, which are based on the results in [84] of the Tesla Model 3.

With the transmission design for all four topologies, the mass and volume are estimated as the first evaluation step. The volume of the components is calculated by applying

$$V_{ges} = \sum_{i=1}^{n} \frac{\pi}{4} (d_i^2 - d_{inner,i}^2) \cdot b_i,$$ (4)

with n describing the number of components, d the outer diameter (d_{inner} the inner diameters, respectively), and b the gear width. The volume of the transmission is calculated based on [56], also taking gaps between housing and gears into account. Considering structure optimization, such as holes in larger gears, a coefficient θ is defined, reducing the volume of the transmission to improve the volume estimation.

The mass of the shafts and gears is calculated by multiplying their volume with the density of the applied material ρ [66]. Bearings and auxiliary masses are considered to be constant. The mass of the housing is calculated by incorporating the air gaps l_a into the bounding box dimensions around the transmission components with w as the transmission width, h its height, and l its length, multiplied by the housing wall thickness t in the following equation:

$$M_{ges} = \rho_{aluminum} \cdot t \cdot 2l_a(w + h + l).$$ (5)

Before the final selection process, the efficiencies, or rather, the power losses, are assessed. To do so, we selected operating points to be analyzed in WTplus and finally summed up into an energy loss for every topology. The selected operating points are the two extreme points of the motor, its highest available torque at top speed, and its corner point. At this point, the energy loss of the transmission is potentially the highest. Additionally, three more points are defined to represent the torque map of the powertrain. With a combination of torque and speed, we selected $\frac{1}{3}$ of their respective maxima and $\frac{1}{3}$ of maximum torque with $\frac{2}{3}$ of maximum speed and reversed. Note: we do not intend to finally assess the powertrain's energy consumption with this estimation rather than differentiate

between the four gearbox topologies as a pre-check. According to the optimization targets and the installation space restrictions, the most suitable transmission topology is chosen.

This transmission is analyzed in detail through the two performance tests, where, from the main simulation program in Simulink, parameters are transferred into WTplus, and the results, such as the required input shaft or rather motor torques and speeds, are fed back into the main program together with the resulting power losses at the respective load points.

2.2.2. Electric Machine

With the required torques and speeds at the transmission input shaft, the electric machine is designed and simulated. This process starts with determining the nominal point, which is then transferred to the design of the electric machine concept, where we provide different approaches for asynchronous motors (ASMs) and permanent magnet synchronous motors (PSMs), which is determined in the pre-initialization step. The applied simulation tool is *Motor-CAD* by *Ansys Inc., Canonsburg, PA, USA* [85].

In order to achieve a vehicle-oriented design, the determination of the nominal point is chosen in dependence on the vehicle parameters. The nominal point is defined through torque and speed and corresponds to the corner point of the continuous load curve. Two different methods are implemented: The first approach is based on [43], where the nominal point is chosen depending on the drive cycle. The second approach considers the maximum velocity and acceleration.

Considering the drive cycle (approach 1), velocity v_{cycle} and acceleration a_{cycle} are converted into machine torque and rotational speed. The corner torque is set in relation to the maximum torque in the cycle, which can exceed the corner torque by an overload factor $K_{OL,1}$. The corner rotational speed is initialized with 21,000 rpm and iteratively lowered until the torque with the highest distance to the continuous load curve is a multiple of the overload factor $K_{OL,2}$. The load curve is set to have a constant torque of T_{corner} until the corner speed n_{corner} is reached and then decreases proportionally to $\frac{1}{n^2}$.

The second nominal point determination utilizes target values of the maximum velocity v_{max} and acceleration a_{max}. The latter is given as an acceleration time t_a needed to reach a defined velocity v_{target}. From v_{target}, which is commonly set to $v_{target} = 100 \frac{\text{km}}{\text{h}}$, a rotational speed is derived, the potential corner speed $n_{corner,a}$. The maximum torque is derived using the targeted acceleration ($a_{target} = \frac{v_{target}}{t_a}$ and a ratio between the maximum torque T_{max} and the permanently available corner torque T_{corner}, which is set to $\frac{T_{max}}{T_{corner}} = 3$ initially.

After the nominal point determination, the selected electric machine type is designed. For the asynchronous motor (ASM), the design is based on [86] with its structural layout shown in Figure 3a and follows an analytical approach, where a pre-design is followed by a detailed design, in which feedback loops are implemented to optimize the electric machine within the given design parameters. These feedback loops follow the analytical recalculation, Motor-CAD recalculation, and thermal recalculation modules. If the thermal recalculation is sufficient, the machine design is completed. This module delivers substitute circuit diagram parameters, the maximum torque depending on the speed, the thermal envelope, the efficiency map, and the inductivities depending on the operating point as outputs. The substitute circuit parameters and inductivities are required for the power electronics design. The efficiency map allows a faster calculation of the energetic efficiency during drive cycle simulation. Also, the mass and dimensions of the ASM are calculated within the Motor-CAD environment and fed into this tool.
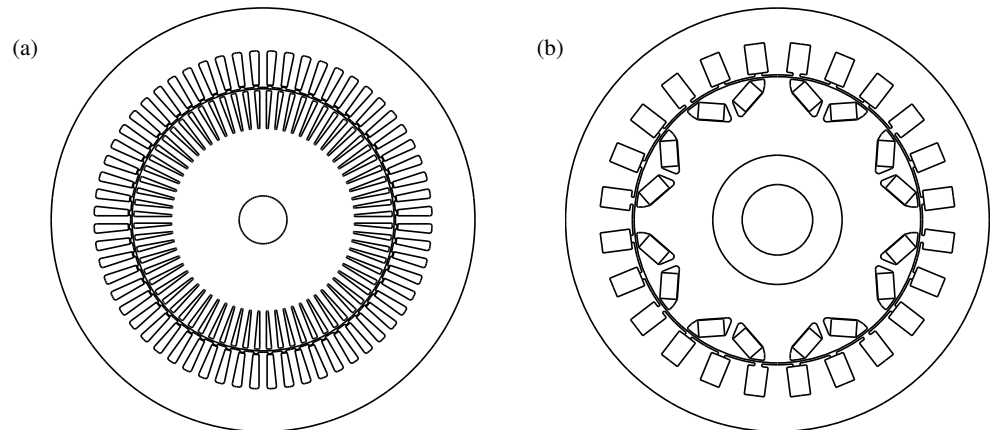
Figure 3. Electric machine layout concepts from Motor-CAD. (**a**) asynchronous motor and (**b**) permanent magnet synchronous motor layout.

The permanent magnet synchronous motor (PSM) design consists of a less analytical approach since an analytical calculation of magnetic stray fields is not feasible. This, on the one hand, allows for a greater variety of concepts, but on the other hand, delivers more insufficient results where the simulation in Motor-CAD might be aborted. For the PSM design, we use the *e4a* template from Motor-CAD as a base, shown in Figure 3b, which is designed for a battery voltage of $U_{Batt} = 720$ V and a peak power of $P_{PSM} = 145$ kW. It represents a machine of eight poles, a V-shaped magnet arrangement, and hairpin windings. As hairpin windings are typically designed in an even number of layers, the number of winding layers (design parameter) is restricted to two, four, and six.

In the initialization step with the gear ratio, the desired acceleration, and the vehicle configuration, a desired maximum torque, $T_{max,desired}$, and the corresponding corner speed, $n_{corner,desired}$, are calculated. Based on a simplified speed–torque curve, with the torque estimated to be constant until n_{corner} and then dropping off hyperbolically, the desired torque is checked to be within this curve. If not, the requirements are not met, and thus, the simulation is aborted for this respective parameter configuration. Otherwise, the e4a template is updated with the parameter configuration and generated in Motor-CAD. The mass, outer diameter, and length of the machine are accessed and saved in the output. Further, an efficiency map is generated for the drive cycle simulation, and the equivalent circuit parameters (ECPs) are calculated for the power electronics design. Additionally, the maximum speed and acceleration are calculated and saved.

There are four different approaches to simulating the behavior of the electric machine in drive cycles. The first is applying analytical equations. This option requires low computational effort but neglects the thermal monitoring of the windings. Further, it is limited to the ASM type, and the efficiency calculation is based on empirically calculated ECPs, which eventually are not sufficiently accurate.

The remaining three approaches utilize the Motor-CAD functions with the fundamental advantages of an implemented thermal model and optimized computational accuracy. The first option is the *duty–cycle* function in the *Lab model*. It comes with fast computational time combined with the other approaches and thus is used in the thermal recalculation of the ASM.

The other two approaches include Motor-CAD in the vehicle simulation. These optimize dynamic effects, which are important considering battery voltage variations during drive cycles. One option to implement this is with a functional mock-up unit (FMU) block in Simulink. As this method leads to problems when compiling the Simulink model, the fourth method is chosen for this project. A specific Simulink block is implemented,

which hands the inputs over to Motor-CAD, starts calculating the respective operating point, extracts the results, and outputs them.

2.2.3. Power Electronics

The results from Motor-CAD of the electric machine module are then transferred into the power electronics module, which is directly computed in Simulink. The mechanical demands at the motor shaft and the ECPs are fed into the *motor control* model, which calculates the required voltage, current, and power factor using the Park and Clark transformation [87]. These are the inputs for the *power electronics* model, which ultimately converts the AC to DC parameters for the high-voltage battery. The power electronics model also calculates the total power, the power loss, and the junction temperature for the simulation.

The power electronics module has limited design parameters, as it is the critical interface between the electric machine and the high-voltage battery module. The motor control module provides algorithms with flexible application to different ECPs, which are changing due to different parameters in the electric machine module. The modeling of the power electronics is based on datasheets of the respective manufacturers [88,89]. Similar to the electric machine, the type of switches is pre-selected in the pre-initialization step: IGBT or silicon carbide (SiC)-metal–oxide–semiconductor field-effect transistor, and the number of parallel-connected switches.

In most studies, static ECPs are used for the control model; however, in reality, ECPs are constantly changing, mainly resulting from the saturation effects in the electric machine [90]. Therefore, we implemented parametric modeling based on varying ECPs.

For the ASM module, three different ECPs are influenced by the saturation effect. The magnetizing inductance L_m, the stator leak inductance L_{ls}, and the rotor leak inductance L_{lr} [91]. The latter two are small compared with the first and hence do not influence the dynamics of the stator inductance L_s, the rotor inductance L_r, and the leakage coefficient σ. Therefore, L_{ls} and L_{lr} are kept constant, and only L_m is considered a dynamic parameter for modeling an ASM. The dynamic ECPs of the ASM depend on current changes through varying torque and speed. With the *Efficiency map* feature in Motor-CAD, results for L_m are identified over the entire operating range. The step size for this application was chosen at 30 rpm and 1 Nm for decent accuracy. In the PSM module, the saturation effect impacts three dynamic ECPs. The permanent magnetic flux linkage ψ_{pm}, the d-axis inductance L_d, and the q-axis inductance L_q [92]. The values are obtained analogously to the ASM.

For the rated area in the ASM, the current feedback (CF) and maximum torque per ampere (MTPA) control strategies are used, whereas in the PSM, the $-i_d = 0$ and MTPA strategies are used. After the voltage limit for the voltage source inverter (VSI) is reached, in both machine types, field weakening control is applied [93]. The inverter model calculates the losses and junction temperature using the equivalent circuit thermal model and the DC demand delivered by the high-voltage battery.

The loss models are divided into a loss model for the IGBT and one for MOSFET types. Starting with the IGBT loss model, an IGBT switch consists of an IGBT unit (collector-emitter) and its anti-parallel diode, which are operating cyclically in on–off states. The losses generated comprise the conduction losses P_{cond} and the switching losses P_{sw} [94]. The IGBT model is modeled based on the data of the *FS820R08A6P2B* component by *Infineon Technologies AG, Neubiberg, Germany* [88], which is used in the Volkswagen ID.3 [63].

The losses for a B6-VSI module with IGBT switches are expressed through the following equations:

$$P_{\text{cond,IGBT}} = v_C \sqrt{2} I_{\text{phase,RMS}} \left(\frac{21}{\pi} + \frac{m_a \cos \theta}{8} \right) + 2R_C I_{\text{phase,RMS}}^2 \left(\frac{1}{8} + \frac{m_a \cos \theta}{3\pi} \right), \quad (6)$$

$$P_{\text{cond,Diode}} = v_D \sqrt{2} I_{\text{phase,RMS}} \left(\frac{21}{\pi} - \frac{m_a \cos\theta}{8} \right) + 2 R_D I_{\text{phase,RMS}}^2 \left(\frac{1}{8} - \frac{m_a \cos\theta}{3\pi} \right), \quad (7)$$

$$P_{\text{sw,IGBT}} = f_{\text{s,IGBT}} (E_{\text{on,IGBT}} + E_{\text{off,IGBT}}), \quad (8)$$

$$P_{\text{sw,Diode}} = f_{\text{s,IGBT}} (E_{\text{on,Diode}} + E_{\text{off,Diode}}), \quad (9)$$

$$P_{\text{inv,loss}} = 6 (P_{\text{cond,IGBT}} + P_{\text{cond,Diode}} + P_{\text{sw,IGBT}} + P_{\text{sw,Diode}}), \quad (10)$$

with m_a as the modulation index in space vector pulse width modulation (SVPWM) expressed through

$$m_a = 2 \cdot \frac{\sqrt{2} V_{\text{phase,RMS}}}{V_{DC}}. \quad (11)$$

Infineon introduced a method for determining v_C, R_C, v_D, and R_D [95]. These values are obtained by linearization of the manufacturer's datasheet. As the datasheet indicates, the test boundary conditions were set at 25 °C to 175 °C, and the curves corresponding to these temperatures were linearized. The reference values for v_{C0} and v_{D0} were obtained from the linearized curves. A safety margin of 1.1 to 1.2 is typically used for engineering applications.

The loss model for the SiC-MOSFET module is rather divided into two conditions than in on–off states. If $I_{\text{phase,RMS}} \cdot R_{\text{DS,on}} \leq v_{\text{D,plateu}}$, the losses are calculated as follows, while diode losses are neglected [36,96,97]:

$$P_{\text{cond,SiC}} = R_{DS(\text{on})} I_{\text{phase,RMS}}^2, \quad (12)$$

$$P_{\text{sw,SiC}} = f_{s,\text{SiC}} (E_{\text{on,SiC}} + E_{\text{off,SiC}}). \quad (13)$$

If $I_{\text{phase,RMS}} \cdot R_{\text{DS,on}} > v_{\text{D,plateu}}$, the anti-parallel diode conduction is triggered and the losses are calculated as follows [36,97]:

$$P_{\text{cond,SiC}} = 2 R_{\text{DS,on}} I_{\text{phase,RMS}} \left(\frac{1}{8} + \frac{m_a \cos\theta}{3\pi} \right), \quad (14)$$

$$P_{\text{cond,Diode}} = v_{\text{D,plateu}} \sqrt{2} I_{\text{phase,RMS}} \left(\frac{1}{2\pi} - \frac{m_a \cos\theta}{8} \right) + 2 R_D I_{\text{phase,RMS}}^2 \left(\frac{1}{8} - \frac{m_a \cos\theta}{3\pi} \right), \quad (15)$$

$$P_{\text{sw,SiC}} = f_{s,\text{SiC}} (E_{\text{on,SiC}} + E_{\text{off,SiC}}), \quad (16)$$

$$P_{\text{sw,Diode}} = 0, \quad (17)$$

which ultimately concatenate in the equation for the inverter power loss to

$$P_{\text{inv,loss}} = 6 \cdot n_p (P_{\text{cond,SiC}} + P_{\text{cond,Diode}} + P_{\text{sw,SiC}}), \quad (18)$$

where $P_{\text{cond,Diode}} = 0$ for the first case, in which the diode is in blocking mode and n_p for the number of parallel connections. For the SiC-MOSFET module, we apply data from the *SCTW100N65G2AG* module by *STMicroelectronics N.V., Plan-les-Ouates, Switzerland* [89], which is used in the Tesla Model 3 [84]. The linearization of R_D, E_{on}, and E_{off} for the SiC-metal–oxide–semiconductor field-effect transistors loss model was performed similarly to the IGBT model. For the calculation of $R_{\text{DS,on}}$ and $v_{\text{D,plateu}}$, we applied the method derived from [97].

The thermal behavior of the inverter module is modeled through an equivalent circuit model. For the IGBT type, there are four RC links, composed of thermal resistances $r_{th,JC}$, and capacities $C_{th,JC}$, connecting the junction to the case with values based on the datasheet [88]. Every resistor and capacity (RC) link is modeled by a Simulink Parallel RLC Branch block; they are connected in series to create the thermal model based on the work of Chan et al. [36]. For the SiC–metal–oxide–semiconductor field-effect transistors module, the manufacturer provided a total thermal resistance of $r_{th,JC} = 0.42 \frac{°C}{W}$ and did not include thermal capacitance [89]. Therefore, only one parallel RLC branch block is used.

2.2.4. High-Voltage Battery

The final module, the high-voltage battery, starts with the DC demands given by the power electronics module. In this module, an internal program in Simulink is used called *Simscape battery* applying the thermal library [98]. In the first step, the specified parameters and settings are collected. The settings are similar to the electric machine or the inverter type, which are set before starting the optimization framework, such as the system voltage of the battery pack, which is either set to $U_{Batt} = 400$ V or $U_{Batt} = 800$ V. Similar to the transmission module, additional parameters are not varied in the optimization module but rather optimized within this module. These parameters are the number of parallel modules on the system level, the number of parallel cells on the module level, the number of serial modules on the system level, the number of serial cells on the module level, and the cell chemistries. The following five steps are based on [14] for the pre-design of electrical battery systems for BEVs. The design parameters mainly refer to the used cells. After the cell data are loaded, considering all the pre-selected parameters and the computed outputs of the component modules, in the third step, potential module configurations are designed and compared with the vehicle requirements in the fifth step. Modules that do not meet the requirements are sorted out. The remaining modules are used in the next step to build battery packs, which are also checked against the requirements. The remaining battery packs, which have not been sorted out, are extended by a battery thermal management system (BTMS), which includes a spatial adjustment of the battery pack. After the final requirement check, battery packs that do not fulfill all of the requirements are discarded. This differs from the procedure for the ASM design module, where the procedure is looped and parameters are slightly changed. Here, all potential configurations within the boundaries are computed rather than only one. From the remaining battery packs, the one with the lowest mass is chosen for further simulation. The mass has been chosen as the main criterion because it is directly relevant to the resistance forces while driving and, thus, energy consumption, which is the main evaluation objective in this study. Ultimately, the designed battery pack is the output of the simulation framework.

After the battery pack design module, the pack with the lowest mass is simulated to analyze vehicle loads and optimize the system iteratively. The simulation enables the analysis of dynamic characteristics, thermal reactions, the overall performance of the battery pack, and the evaluation and optimization of the overall concept. Simscape was chosen as a physical model environment based on its functional range, its flexibility, and the good accessibility of the simulation environment.

In addition to the data from the battery design, battery simulation settings shown in Table 1 are required. With this information, a battery library is created whose structure and wiring are analogous to the battery design. Pre-defined settings decide the depth of the modeling. A dissipative state of charge equalization does not require high computational power, and as it is state-of-the-art, it's strongly recommended. Local resolution of the model is selected considering the respective development phase. To reduce computing time, an initially condensed examination of the cells is followed by higher resolution to analyze the

thermal behavior of each cell in the later stages of the concept development. The user also specifies if the cells are modeled with a static resistance or with RC links for the dynamic part. Any number of RC links between one and five work, but two is recommended [20].

Table 1. Overview of the high-voltage battery module's simulation settings.

Parameter	Unit	Range
SOC equalisation strategy	-	None, dissipative
Local resolution	-	Integrated, grouped, detailed
Number of RC circuits	-	R, rc1, rc2, rc3, rc4, rc5
Ambient temperature	$^\circ$C	$[0, \infty]$
Time step size	s	$[0, \infty]$
Manufacturer parameterisation	-	0, 1
Over current factor racemode	-	0, 1

The battery pack is then initialized with the values corresponding to the chosen cell, and the battery pack model is integrated into the simulation framework, where the ambient temperature is used as the start temperature of the battery pack and the cooling liquid. With the data fed back into the simulation framework, two performance tests are implemented, as mentioned before.

3. Results and Discussion

After the detailed explanation of the simulation framework and the component design modules, we present the tool's capabilities. But before optimizing a respective electric vehicle concept, we validate our simulation model. To do so, we set all parameters to fit the Volkswagen ID.3, which was torn down and comprehensively analyzed [63]. After the validation, we show the optimization framework for an exemplary vehicle and discuss its functionalities and results. Finally, we take a closer look at the computation time and potential optimization strategies to improve or rather decrease computational effort.

3.1. Validation

The parameter configuration of our simulation framework to meet the Volkswagen ID.3 data is shown in Tables A1, A3–A5 in the last column. The cycle chosen is the WLTP class 3. The cells from the real-world measurements are selected. The starting state of charge (SOC) was set to 96% to match the experimental data. The electric machine was adapted from the e4a template in Motor-CAD to match the Volkswagen concept. The optimization framework is included, while the boundaries were set to allow only for the desired parameter, and the NSGA-II parameters were set for a single run.

With the dynamometer tests on the vehicle level, the VW ID.3 achieved an energy consumption of an average of 13.16 $\frac{\text{kWh}}{100\text{km}}$. In contrast, the simulated vehicle exceeded this result with an energy consumption of 12.89 $\frac{\text{kWh}}{100\text{km}}$. Considering a battery capacity of 63 kWh for the actual vehicle, with data collected from the Certificate of Conformity (CoC) according to EU Regulation 2018/858 [99], and 61.48 kWh for the simulation model, this results in an estimated total electric range of 478.72 km for the real vehicle and 476.96 km for the simulated vehicle. Both electric range results are higher than the electric range of 408 km given by the manufacturer in the CoC, which results from differences between the gross and net capacity. Figure 4 proves the behavior of both the dynamometer test and the simulation are concurring.
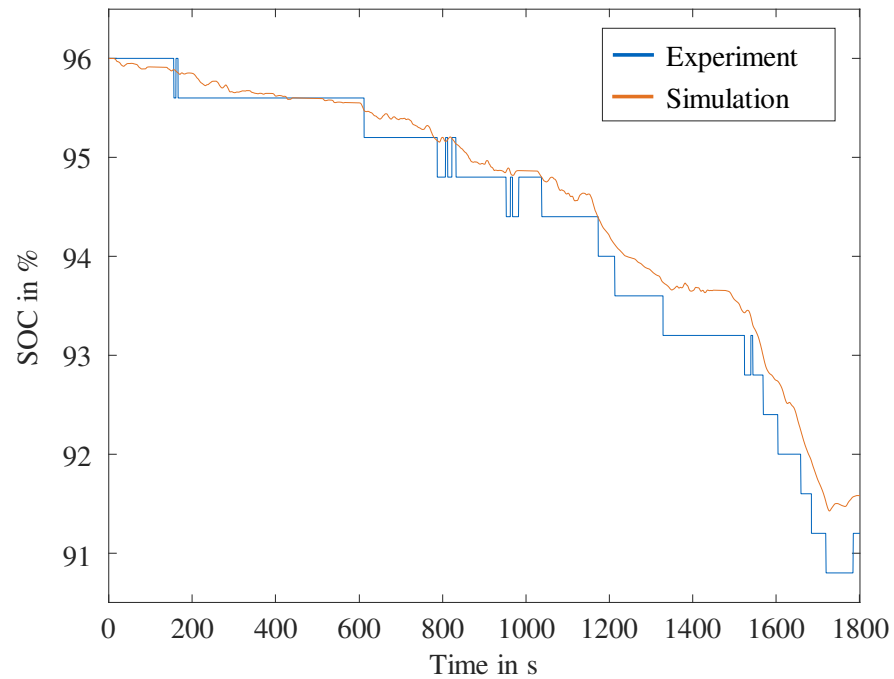
Figure 4. SOC behavior between the dynamometer test and simulation on vehicle level.

From the vehicle level backward through the component level, the high-voltage battery is the first module. The battery efficiency for the experiments was derived from the ohmic resistance with a value of 1.8 mΩ [63]. As seen in Figure 5, the efficiencies are similar. Especially in the high-speed parts of the Worldwide Harmonized Light Vehicles Test Cycle (WLTC), the drive cycle of the WLTP, efficiencies tend to have larger differences. This is explained by higher currents and thus squared power losses, while mechanical power increases linearly.
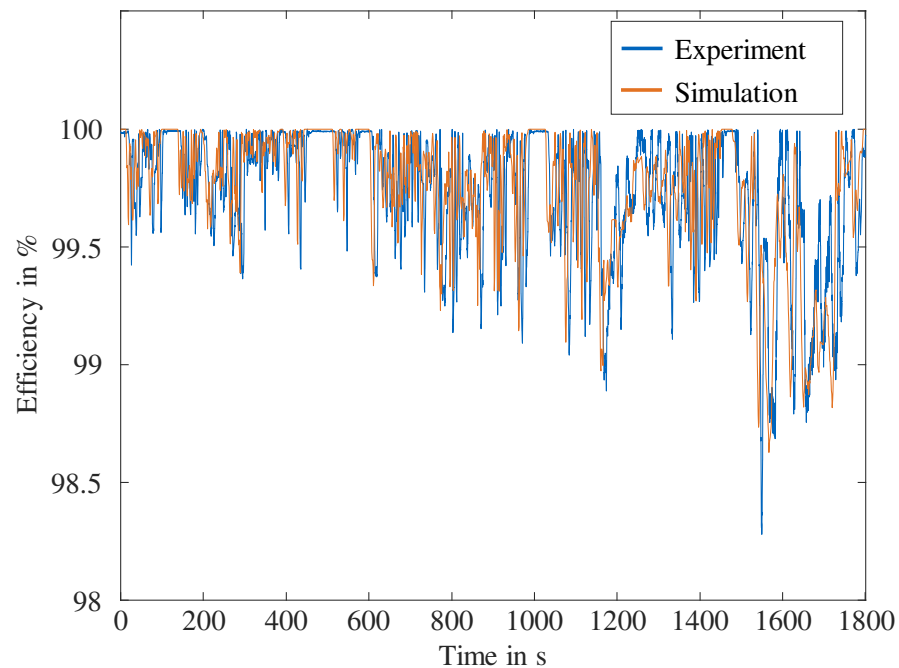

Figure 5. Efficiency behavior between the dynamometer test and simulation of the battery module.

From the high-voltage battery to the power electronics module, an average electrical power of 5.79 kW for the dynamometer experiments during the WLTC is measured. The average electrical power in this simulation framework is 5.72 kW with an MTPA

control implemented, which results in an error of 1.21%. Also, for the inverter losses, the dynamometer experiment reached an average loss of 275.14 W while the simulation framework computes an average loss of 272.35 W. This leads to a derivation of 1.01%.

The validation of the mechanical components is more difficult since the dynamometer tests do not distinguish between the electric machine and the transmission, as the dynamometer tests provide only the inverter power P_{inv} and the mechanical power at the wheels P_{mech}. Therefore, the validation consists of two approaches: First, the simulation model is compared with the work of Humphrey et al. [100]. In this study, gearboxes with different finishing technologies, such as diamond-like carbon, super-finish steel, and standard steel, are evaluated.

The investigated model is based on a two-stage, single-speed gearbox similar to the topology used in the VW ID.3 and topology one in this study, where the test was performed on the New European Driving Cycle (NEDC). We rebuilt their model with the transmission module in this simulation framework and investigated the friction losses, as only the friction losses were investigated in [100]. The average transmission friction loss result was 218 W compared with 224.22 W in this study's model, resulting in a derivation of 2.85%. In the second approach, it is presumed that the difference between P_{inv} and P_{mech} equals the sum of the transmission losses $P_{\mathrm{trans,loss}}$ and the electric machine losses $P_{\mathrm{motor,loss}}$. Table 2 shows these results and the previously presented comparisons as an overview. The rather small deviations prove the validation of our simulation framework, which means the numerical component module provides adequate results.

Table 2. Overview of the validation process with comparisons of the vehicle dynamometer tests in [63] and the results of the presented simulation framework during a WLTC.

Domain	Dynamometer Test	Simulation Framework	Deviation
Electric range	478.72 km	476.96 km	0.37%
Battery efficiency	83.28%	83.55%	0.32%
Electrical power	5.79 kW	5.72 kW	1.2%
Inverter loss	275.14 W	272.35 W	1.01%
Transmission power loss [100]	218 W	224.22 W	2.85%
Transmission loss	-	396 W	-
Electric machine loss	-	545 W	-
Mechanical power	4.82 kW	4.78 kW	0.83%
Mechanical loss	968 W	941 W	2.79%

3.2. Simulation Tool Results

With the component design modules proven to deliver meaningful results, the entire simulation framework is investigated in the following section. This exemplary optimization tool run is divided into two parts: First, we will show exemplary results for single objectives to discuss the functionality of our methodology, and second, we will compare four vehicle concepts with different parameter configurations.

3.2.1. Optimization Framework Results

First, we want to point out that the presented results do not intend to prove the functionality of the optimization since the NSGA-II is well tested and the common algorithm for such a use case [70–72]. To reduce computational effort and simulation time, we apply our framework to explore a design space with a small population size and a number of generations of 15 on the WLTC with its high-speed part instead of performing a holistic optimization. This leads to 225 simulations, which compute for about three weeks in its initial state, performed on a standard consumer laptop with an Intel i7 processor and 16 GB of random access memory (RAM). Computation optimization strategies will be discussed

in Section 3.3. The performed test achieved 204 successful runs, where 13 failed during the simulation of the drive cycle, six failed the transmission pre-check, and two failed the electric machine pre-check. The 204 successful simulations showed reasonable results, for example, simulation number 52. The resulting vehicle concept is equipped with a high-voltage battery in a *120s2p* configuration and a module configuration of *10s1p*, resulting in a battery capacity of 68.31 kWh and a transmission gear ratio of 10.99. This leads to an energy consumption of 17.32 $\frac{kWh}{100km}$ and an overall electric range of 394.4 km. Although this might look quite small, considering the cycle is restricted to the high-speed phase, this is a good result. Further requirements of a top speed of 160 $\frac{km}{h}$ and an acceleration time of < 7.3 s have been met with a top speed of 275 $\frac{km}{h}$ and 5.07 s in reaching the 100 $\frac{km}{h}$ from a standstill. Note that this is a powertrain design for an early development phase, which will change during further refinement. Thus, at this stage, the results might occur optimistically but deliver a founded starting point and help to understand parameter configurations and tendencies of specific parameters for a specific vehicle concept.

To further demonstrate the functionality of the powertrain optimization tool, a calculation of the NSGA-II with a population size of 10 was carried out over eight generations. Of these 80 simulations, 16 failed during the drive cycle, 13 failed in the battery pre-check, and eight failed in the transmission pre-check, which leaves 43 remaining successful simulated vehicle configurations, giving a statistically meaningful dataset for the following observations. For a better comparison, we restrict the results to the *2p* battery system configurations.

As seen in Figure 6a, there is an inversely proportional correlation between the vehicle's energy consumption and its range. This is an intuitive correlation, as the battery capacity varies between 62.68 kWh and 68.38 kWh, resulting in a high impact on the energy consumption and its electric range. For different system voltage levels of the battery, 432–438 V (blue), 409 V (grey), and 402 V (green), three different trendlines, each with a R^2-value greater than 0.99, are identified.
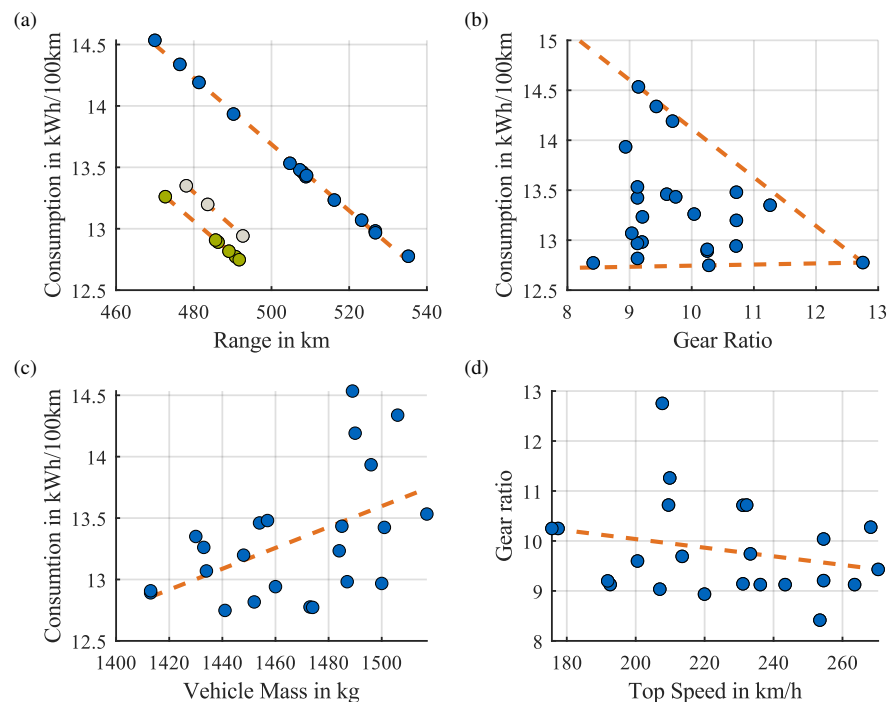

Figure 6. Simulation results of single parameter configurations evaluated against the energy consumption on vehicle level. (**a**) shows the achieved range, in (**b**) different gear ratios are displayed, (**c**) evaluates the vehicle mass, and in (**d**) the achieved top speed is considered.

The transmission gear ratio influences the vehicle's energy consumption significantly. While low gear ratios spread energy consumption, higher gear ratios tend to lead to lower energy consumption with an optimum at both lines crossing, shown in Figure 6b.

Similarly to the vehicle's range, the vehicle mass correlates with the energy consumption. Since higher vehicle masses imply higher rolling resistances and thus higher resistance forces at the wheel, this results in higher energy demands to overcome this resistance. The connection between electric range and vehicle mass lies in the battery capacity; higher battery capacity is most likely based on more cells and, therefore, larger and heavier battery packs. The correlation between vehicle mass and energy consumption with $R^2 = 0.2538$ is illustrated in Figure 6c. This, on the other hand, proves that the remaining powertrain components also influence the vehicle mass. As the maximum rotational speed of the electrical motors is limited, the gear ratio has a significant impact on the vehicle's top speed. For that reason, original equipment manufacturers (OEMs) must find a compromise between the desired acceleration and top speed of the vehicle in single-speed transmission designs. As presented in Figure 6d for the performed run, lower top speeds are less influenced by the gear ratio, but increasing top speeds requires lower gear ratios.

3.2.2. Vehicle Concept Comparison

Now, four vehicle concepts that were configured during this exemplary simulation are further analyzed. This intends to show the variability of the simulation framework and the diversity of the different results. Their detailed parameter configurations are concatenated in Table A6 in Appendix C for the vehicle level, the battery, the electric machine, and the transmission. Despite the PSM being more common, we focused on the PSM in this run since the PSM reached better results, especially for the gravimetric energy density. Still, more importantly, it reached more variations in single results based on its less restrictive design approach. A first look at the table proves the variety of the results, with large deviations in single categories and, thus, a great variety of different powertrain design concepts.

Vehicle 1 shows a high overall energy consumption of 14.53 $\frac{kWh}{100km}$. The reason for this is shown in Figure 7a since the designed combination of the electric machine and transmission (low gear ratio of 9.14) transfers the cycle's load points into rather less efficient areas in the electric machine's efficiency map. Note that there are many critics of the WLTP claiming its velocity profile is less realistic. Therefore, even though the vehicle's energy consumption is evaluated through the WLTC, the electric powertrain components should not be designed to optimally fit this cycle. That is why we also consider the acceleration time and the vehicle's top speed as requirements.

Compared with the efficiency map of vehicle 1 on the left side of this figure, vehicle 4 shows more load points in operating regions of higher efficiency, leading to a low overall energy consumption of 12.78 $\frac{kWh}{100km}$ in Figure 7b. This is explained by the high gear ratio of 12.75 shifting the motor operating points to higher shaft speeds, where it is more efficient. The second effect of the high gear ratio is the lower top speed of 207.72 $\frac{km}{h}$ compared with the 231.12 $\frac{km}{h}$ of vehicle 1. The two efficiency maps also show the diversity of the electric machine design, where different machine characteristics are constructed for both the maximum torque curve and efficiency areas.

Due to the high efficiency of the powertrain, vehicle 4 with a consumption of 12.78 $\frac{kWh}{100km}$, it reaches a higher electric range than the other three vehicles with 535 km over 470–476 km, while having a total capacity of 68.38 kWh, similar to vehicle 1 and vehicle 3 with 68.31 kWh. Vehicle 2 achieves a similar range as vehicles 1 and 3 while only having a capacity of 62.68 kWh due to its low consumption of 13.26 $\frac{kWh}{100km}$ compared with 14.53 $\frac{kWh}{100km}$ in vehicle 1 and 14.34 $\frac{kWh}{100km}$ in vehicle 3.
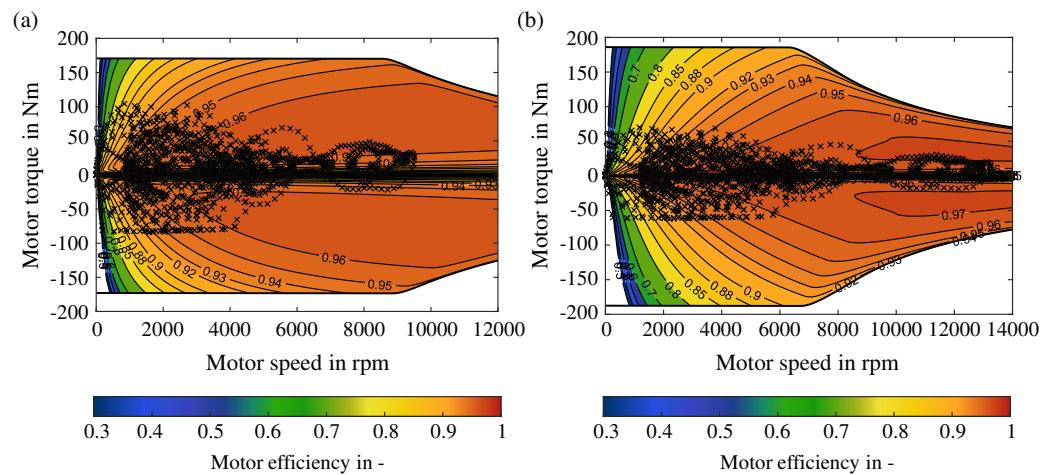
Figure 7. Efficiency maps of vehicle concepts designed within the simulation framework with the load points converted of the selected WLTC. (**a**) Efficiency map of vehicle 1 and (**b**) of vehicle 4.

3.3. Simulation Computation and Optimization Strategies

Concluding the results section, we take a closer look at the computation time for the simulation framework. Following the discussion of a new vehicle concept, a notable delay typically occurs before the respective divisions begin their development processes and exchange preliminary results. Nonetheless, as mentioned before, the initial stage of our simulation requires high computational time, especially in the last performance test, the energy consumption investigation during the official WLTP. In addition to the estimation presented before with the exemplary simulation run, a single parameter configuration takes up to 4.5 h of computation. To further reduce this computational effort, we present strategies that optimize and rather decrease simulation time.

First, within every component design module, we included pre-checks to either avoid simulating infeasible or less effective parameter configurations or optimize parameter configurations slightly. These pre-checks intend to investigate the model's capability to perform the drive cycle. These are explained in detail in the respective component modules. The main objective behind the pre-checks is to allow for a wide range of design parameters, providing a wide space of potential results and thus improving the chances for the NSGA-II algorithm to find the global rather than a local optimum.

Another form of the pre-check is the acceleration cycle. During the simulation of the acceleration time from a standstill to a defined vehicle velocity, we observe whether the vehicle meets the requirements for the investigated vehicle concept before the computationally intensive drive cycle is run. Also, to account for a reasonable computation time in combination with achieving meaningful results, a step size of 1 s has been set.

Also, we included a Simulink function wrapper. This optional function checks if the parameter configuration has been run before. Although it is unlikely that the NSGA-II algorithm picks the same configuration twice, there is the option to set a threshold for each design parameter. If the new configuration lies within this threshold, the drive cycle simulation is bypassed.

Similar to the function wrapper, we implemented an electric machine library. This aims to reduce costly simulation time within Motor-CAD. Although the design parameter design varies with every optimization, or, rather, every vehicle concept under investigation, there is a certain range of parameters that occurs in many vehicle concepts. To avoid simulating electric machine parameter configurations that have already been simulated, every potential and feasible parameter configuration and its simulation results are transferred to the library. This library is checked before the simulation parameters are transferred to Motor-CAD,

and if available, results will be taken before repeating the simulation. This library and the function wrapper are cross-project-based and, thus, not only within one optimization.

4. Summary and Conclusions

This study presents a holistic simulation framework for the electric powertrain design in an early development phase. By applying state-of-the-art numerical simulation tools, we ensure achieving state-of-the-art results that are the foundation of further development in respective divisions. Aiming for an overall holistic starting point in powertrain development, adaptations in component divisions are independent of other components, and thus, this tool optimizes development time. The major discoveries of this study can be summarized as follows:

- **Validated electric powertrain simulation framework.**
  To validate our simulation framework and prove its functionalities and that the results obtained from the component design modules are meaningful, we investigated a defined parameter configuration obtained from a vehicle teardown and dynamometer tests in [63]. The deviations within the results show the implemented modules design state-of-the-art electric powertrain components and thus provide meaningful results.
- **Design space exploration and modular framework.**
  The simulation framework allows for multiple applications. First, with specific parameter configurations, the tool allows for the analysis of single objectives, such as exploring the design space of respective design parameters or identifying the sensitivity or impact of these parameters. Besides the design parameters, the modularity of our simulation tool enables users to append the framework with their own component design modules or select modules with less computational effort if certain components do not require detailed results.
- **Optimization approach for vehicle concepts.**
  The main functionality of this framework is the optimization approach. This aims to find an optimal starting point for a specific vehicle concept to set the foundation for further development. The framework's modularity is also applicable within the optimization, allowing for reduced computational effort while investigating a specific component or parameter. The optimization in this study applies an NSGA-II algorithm and is set for a multi-objective optimization approach, whereas we focused on energy consumption or, rather, efficiency.
- **Optimization strategies reducing computation time.**
  This framework is used at the beginning of a development process to provide a foundation for a new or updated vehicle concept. To provide users with results earlier, we present strategies that intend to reduce computational time.

Author Contributions: N.R.: Conceptualization, Methodology, Investigation, Resources, Writing—Original Draft, Visualization, Writing—Review and Editing, Project administration. N.R. is the first author. S.D.: Investigation, Writing—Original Draft, Writing—Review and Editing, Visualization. J.K.: Writing—Review and Editing, Visualization. M.L.: Resources, Supervision, Writing—Review and Editing, Funding acquisition. All authors have read and agreed to the published version of the manuscript.

Appendix A. Vehicle Concept Parameters

The vehicle concept parameters of the overall simulation framework in Section 2.1 are divided into the vehicle requirement parameters Table A1, which define the targeted vehicle, and into the evaluation parameters Table A2, on which the simulation models are assessed.

Table A1. Overview of the vehicle concept parameters on the vehicle level that define the targeted vehicle with the Volkswagen ID.3 data according to [63].

Parameter (Unit)	Recommended Range	VW ID.3
Range goal (km)	[205, 558]	416
Maximum speed ($\frac{km}{h}$)	[130, 230]	160
Zero to corner speed (s)	[4.05, 12.25]	7.3
Corner speed ($\frac{km}{h}$)	[80, 130]	100
Body type (-)	A - F	C
SUV flag (-)	[0; 1]	0
Driving cycle (-)	-	WLTP_class_3
Motor type (-)	[IM; PSM]	PSM
Inverter type (-)	[IGBT; MOSFET]	IGBT

Table A2. Overview of the vehicle optimization parameters that are evaluated within the result evaluation module.

Parameter	Description	Unit
total_energy	Total vehicle consumption in relation to distance	$\frac{kWh}{100km}$
SOC_diff	Difference between start and end SOC	-
cost	Total powertrain cost, estimated for production in Germany	€
mass	Total powertrain mass	kg
volume	Total powertrain volume	m^3
battery_height	Battery height including battery management system	mm
max_speed	Top speed estimated, according to motor initialization	$\frac{km}{h}$
max_acceleration	Maximum acceleration according to the motor initialization	$\frac{m}{s^2}$

Appendix B. Component Design Parameters

The vehicle and component parameters that are utilized within the optimization and respective component modules are divided into the constant parameters Tables A3 and A4, which do not change within one vehicle concept optimization and the design parameters Table A5, that are changed and optimized in every optimization run with both set to meet the real vehicle data in [63] for the validation analysis in Section 3.1.

Table A3. Overview of the vehicle concept parameters (vehicle, transmission, and ASM) that are constant during the optimization with the Volkswagen ID.3 data according to [63]. Note, there are more parameters (e.g., for the specific topologies) that are not listed here but explained in detail in the simulation model.

Component	Parameter (Unit)	VW ID.3
Vehicle	Mass driver (kg)	68
	Mass body (kg)	800
	Tire radius (m)	0.335
	Rotating mass factor (-)	1.07
	Air density ($\frac{kg}{m^3}$)	1.225
	Air resistance coefficient (-)	0.267
	Frontal area (m^2)	2.3904
	Rolling resistance coefficient (-)	0.009
	Auxiliary drain (W)	280
	Gravitational acceleration ($\frac{m}{s^2}$)	9.81
	Road surface grip level (%)	100
	Ambient temperature (K)	298.15
	Acceleration capability of the tires (-)	0.8
	Longitudinal battery space (mm)	300
	Lateral battery space (mm)	100
	Vehicle length (mm)	4315
	Vehicle width without mirror (mm)	1805
	Vehicle height (mm)	1558
	Package coefficient for the assembly (-)	1.25
	Total mass vehicle (kg)	1976
Transmission	Efficiency (-)	0.96
	Sigma_SH_min (-)	0.8
	Sigma_SF_min (-)	1
	Power oilpump (W)	120
	e1 - Distance between wall and gear (mm)	10
	Thickness housing (mm)	10
	Rib height (mm)	50
	Lenght of differential (mm)	150
	Density steel ($\frac{kg}{mm^3}$)	0.00000785
	Density aluminium alloy ($\frac{kg}{mm^3}$)	0.00000285
	Mass of bearings (kg)	3
	Mass of differential (kg)	3
	Mass of accessories (kg)	2
	Mass of lubricant (kg)	1
	Width carrier (mm)	10
ASM	Corner speed (rpm)	7500
	Constant power speed range (-)	3
	Maximum to constant Power (-)	2.5
	Reference mass (kg)	52.65
	Maximum speed (rpm)	21,000
	Overload factor 1 (-)	2
	Overload factor 2 (-)	1
	Number of phases (-)	3
	Circuit connection (-)	star
	Mass density iron ($\frac{kg}{m^3}$)	7850
	Security factor (-)	2
	Stator, rotor lamination material (-)	M250-35A
	Armature winding, cage material (-)	Copper (Pure)
	Shaft material (-)	MildSteel
	Insulation material (-)	LORD CoolTherm EP-2000
	Add housing diameter (m)	0.035
	Ambient Temperature for convection (°C)	40
	Maximum stator winding temperature (°C)	160
	Maximum rotor cage temperature (°C)	180

Table A4. Overview of the vehicle concept parameters (PSM, power electronics, and high-voltage battery) that are constant during the optimization with the Volkswagen ID.3 data according to [63]. Note, there are more parameters (e.g., for the power electronics' switches) that are not listed here but explained in detail in the simulation model.

Component	Parameter (Unit)	VW ID.3
PSM	Minimum power desired (kW)	50
	Maximum power desired (kW)	750
	Phases (-)	3
	Copper ratio (-)	0.9
	Conductor separation (mm)	0.15
	Insulation thickness (mm)	0.1
	Tooth tip angle (°)	1
	Maximum current threshold (-)	0.05
	Maximum current exponent (-)	2
	Maximum speed (rpm)	25,000
	Stator winding temperature Lab (°C)	155
	Rotor magnet temperature Lab (°C)	120
	Maximum ratio of maximum to constant torque (-)	4
Power electronics	Switchin frequency (Hz)	5000
	R1 IGBT (Ω)	0.005
	C1 IGBT (F)	0.2
	R1 Diode (Ω)	0.015
	C1 Diode (F)	0.06666
	R MOSFET (Ω)	0.42
Battery	Maximum size in x-direction at pack level (m)	3
	Maximum size in y-direction at pack level (m)	2.3
	Maximum size in z-direction at pack level (m)	0.5
	Maximum mass at pack level (kg)	2000
	Nominal maximum voltage at pack level (V)	400
	Desired maximum deliverable current at packing level (A)	250
	Maximum number of parallel connections at module level (-)	0
	Maximum number of parallel connections at pack level (-)	10
	Connection resistance (Ω)	0.001
	Nominal Voltage on Module level (V)	48

Table A5. Overview of the vehicle concept design parameters that are varied during the optimization and the parameters set to meet the Volkswagen ID.3 data according to [63]. Note that the electric machine parameters are varied within 80–120+% regarding the result in the pre-initialization step.

Component	Parameter (Unit)	Recommended Range	VW ID.3
Transmission	Gear ratio	[6, 12]	11.53
	Gear ratio stage 1	[2, 6]	2.957
	Normal module of stage 1	[1.5, 2]	1.67
	Normal module of stage 2	[2, 2.75, 12]	2.111
	Number of teeth stage 1	[21, 40]	20
	Number of teeth stage 2	[21, 40]	23
Electric machine	Motor Index (library)	-	261
	Stator inner diameter	[0.8, 1.2]	-
	Iron length	[0.8, 1.2]	-
	Rotor tooth width	[0.8, 1.2]	-
	Rotor tooth height	[0.8, 1.2]	-
	Stator back height	[0.8, 1.2]	-
	Stator tooth width	[0.8, 1.2]	-
	Stator tooth height	[0.8, 1.2]	-
Battery	Size factor (kWh)	[−40, 40]	0
	Cell Index	[1, 12]	1
	Voltage factor	[9, 15]	12
	Cell type	[1, 3]	1

Appendix C. Vehicle Concept Comparison

The vehicle specifications compared in Section 3.2.2 are provided in Table A6.

Table A6. Overview of vehicle concept and component specifications for comparison.

Component	Parameter (Unit)	Vehicle 1	Vehicle 2	Vehicle 3	Vehicle 4
Vehicle	Energy consumption ($\frac{kWh}{100km}$)	14.53	13.26	14.34	12.78
	Electric range (km)	469.98	472.67	476.41	535.23
	Mass Vehicle (kg)	1489	1433	1506	1473
	Mass powertrain (kg)	429.92	385.34	443.33	417.25
	Volume powertrain (dm^3)	118	167	193	174
	Max acceleration ($\frac{m}{s^2}$)	2.80	10.74	4.25	9.30
	Top speed ($\frac{km}{h}$)	231.12	254.52	270.36	207.72
Transmission	Gear ratio (-)	9.14	10.04	9.43	12.75
	Longitudinal dimension (mm)	250	290	266	324
	Lateral dimension (mm)	175	255	142	438
	Vertical dimension (mm)	225	223	192	317
	Mass gearbox (kg)	22.32	37.79	20.79	62.28
Electric machine	Max torque (Nm)	217.74	509.94	229.29	282.57
	Max power (kW)	159.61	240.30	168.08	133.16
	Max current (A)	781	1938	564	1249
	Housing diameter (mm)	233.91	203.14	224.27	159.79
	Motor length (mm)	260	363	401	327
Battery	Longitudinal dimension (mm)	1144	1456	1144	1588
	Lateral dimension (mm)	1207	628	1202	628
	Vertical dimension (mm)	162	158	162	158
	Mass battery (kg)	360.43	302.27	360.43	329.75

References

1. Chan, C. The state of the art of electric and hybrid vehicles. *Proc. IEEE* **2002**, *90*, 247–275. [CrossRef]
2. Zhang, Z. *Multivariate Time Series Analysis in Climate and Environmental Research*; Springer: Cham, Switzerland, 2018. [CrossRef]
3. Biresselioglu, M.E.; Demirbag Kaplan, M.; Yilmaz, B.K. Electric mobility in Europe: A comprehensive review of motivators and barriers in decision making processes. *Transp. Res. Part Policy Pract.* **2018**, *109*, 1–13. [CrossRef]
4. European Parliament. 2021/0197(COD): CO_2 Emission Standards for Cars and Vans. Available online: https://oeil.secure.europarl.europa.eu/oeil/en/procedure-file?reference=2021/0197(COD) (accessed on 22 November 2024).
5. Hristov, G.; Zahariev, P.; Borisov, S.; Kyuchukova, D. An educational system for real-time monitoring and evaluation of the parameters of electric vehicles. In Proceedings of the 2016 15th International Conference on Information Technology Based Higher Education and Training (ITHET), Istanbul, Turkey, 8–10 September 2016; pp. 1–5. [CrossRef]
6. Trzesniowski, M. *Powertrain*; Springer Vieweg Wiesbaden: Berlin/Heidelberg, Germany, 2023; p. 536.
7. Neubauer, J.; Brooker, A.; Wood, E. Sensitivity of battery electric vehicle economics to drive patterns, vehicle range, and charge strategies. *J. Power Sources* **2012**, *209*, 269–277. [CrossRef]
8. Dimitropoulos, A.; Rietveld, P.; van Ommeren, J.N. Consumer valuation of changes in driving range: A meta-analysis. *Transp. Res. Part Policy Pract.* **2013**, *55*, 27–45. [CrossRef]
9. Rosenberger, N.; Fundel, M.; Bogdan, S.; Köning, L.; Kragt, P.; Kühberger, M.; Lienkamp, M. Scientific benchmarking: Engineering quality evaluation of electric vehicle concepts. *e-Prime-Adv. Electr. Eng. Electron. Energy* **2024**, *9*, 100746. [CrossRef]
10. Ludwig, C.; Chang, F.; Frost, M.; Schimmel, C.; Prokop, G. Investigation of the Influence of Vehicle Payload on Rollover Behavior. In Proceedings of the 22. Internationational Stuttgarter Symposium, Online, 14 March 2022; Springer Vieweg Wiesbaden: Berlin/Heidelberg, Germany, 2022; pp. 201–219.
11. Elverum, C.W.; Welo, T. The Role of Early Prototypes in Concept Development: Insights from the Automotive Industry. *Procedia CIRP* **2014**, *21*, 491–496. [CrossRef]
12. Köller, S.; Schmitz, V. Systematic synthesis and multi-criteria evaluation of transmission topologies for electric vehicles. *Automot. Engine Technol.* **2022**, *7*, 65–79. [CrossRef]
13. European Union. Regulation No 100 of the Economic Commission for Europe of the United Nations (UN/ECE)—Uniform Provisions Concerning the Approval of Vehicles with Regard to Specific Requirements for the Electric Power Train. Available online: https://op.europa.eu/en/publication-detail/-/publication/fd8e6b47-d767-11e4-9de8-01aa75ed71a1 (accessed on 14 January 2025).
14. Reiter, C. Thermische Vorauslegung Hochbelasteter Batteriesysteme für Elektrofahrzeuge in der Konzeptphase. Ph.D. Dissertation, Technische Universität München, München, Germany, 2020.

15. Pham, X.M.; Bui, G.V.; Pham, H.; Pham, L.H.P. Design Process of Electric Vehicle Power System. *Appl. Mech. Mater.* **2022**, *907*, 101–114. [CrossRef]

16. Epp, A.; Sauer, D.U. Multiperspective Optimization of Cell and Module Dimensioning for Different Lithium-Ion Cell Formats on Geometric and Generic Assumptions. *Energy Technol.* **2022**, *10*, 2100874. [CrossRef]

17. Epp, A.; Wendland, R.; Behrendt, J.; Gerlach, R.; Sauer, D.U. Holistic battery system design optimization for electric vehicles using a multiphysically coupled lithium-ion battery design tool. *J. Energy Storage* **2022**, *52*, 104854. [CrossRef]

18. Baumann, M.; Wildfeuer, L.; Rohr, S.; Lienkamp, M. Parameter variations within Li-Ion battery packs – Theoretical investigations and experimental quantification. *J. Energy Storage* **2018**, *18*, 295–307. [CrossRef]

19. Guo, W.; Sun, Z.; Vilsen, S.B.; Meng, J.; Stroe, D.I. Review of "grey box" lifetime modeling for lithium-ion battery: Combining physics and data-driven methods. *J. Energy Storage* **2022**, *56*, 105992. [CrossRef]

20. Hu, X.; Li, S.; Peng, H. A comparative study of equivalent circuit models for Li-ion batteries. *J. Power Sources* **2012**, *198*, 359–367. [CrossRef]

21. Andre, D.; Meiler, M.; Steiner, K.; Walz, H.; Soczka-Guth, T.; Sauer, D. Characterization of high-power lithium-ion batteries by electrochemical impedance spectroscopy. II: Modelling. *J. Power Sources* **2011**, *196*, 5349–5356. [CrossRef]

22. Lee, U.; Kang, N.; Lee, Y.K. Optimization of module structure considering mechanical and thermal safety of pouch cell lithium-ion batteries using a reliability-based design optimization approach. *J. Energy Storage* **2023**, *72*, 108650. [CrossRef]

23. Schmidt, J.P. Verfahren zur Charakterisierung und Modellierung von Lithium-Ionen Zellen. Ph.D. Dissertation, Karlsruher Institut für Technologie, Karslruhe, Germany, 2013.

24. Luzi, M.; Frattale Mascioli, F.M.; Paschero, M.; Rizzi, A. A White-Box Equivalent Neural Network Circuit Model for SoC Estimation of Electrochemical Cells. *IEEE Trans. Neural Netw. Learn. Syst.* **2020**, *31*, 371–382. [CrossRef]

25. Lee, J.D.; Park, D.H.; Kim, R.Y. Novel Variable Switching Frequency PWM Strategy for a SiC-MOSFET-Based Electric Vehicle Inverter to Increase Battery Usage Time. *IEEE Access* **2022**, *10*, 21929–21940. [CrossRef]

26. Sivkov, O.G.; Novak, M.; Novak, J. Comparison between Si IGBT and SiC MOSFET Inverters for AC Motor Drive. In Proceedings of the 2018 18th International Conference on Mechatronics—Mechatronika (ME), Brno, Czech Republic, 5–7 December 2018; pp. 1–5.

27. Rahman, M.F.; Niknejad, P.; Barzegaran, M.R. Comparing the performance of Si IGBT and SiC MOSFET switches in modular multilevel converters for medium voltage PMSM speed control. In Proceedings of the 2018 IEEE Texas Power and Energy Conference (TPEC), College Station, TX, USA, 8–9 February 2018; pp. 1–6. [CrossRef]

28. Liu, C.; Luo, Y. Overview of advanced control strategies for electric machines. *Chin. J. Electr. Eng.* **2017**, *3*, 53–61. [CrossRef]

29. Peddapelli, S.K. *Pulse Width Modulation: Analysis and Performance in Multilevel Inverters*; De Gruyter Oldenbourg: Berlin, Germany, 2016; p. 210.

30. Xu, Y.; Ho, C.N.M.; Ghosh, A.; Muthumuni, D. A Datasheet-Based Behavioral Model of SiC MOSFET for Power Loss Prediction in Electromagnetic Transient Simulation. In Proceedings of the 2019 IEEE Applied Power Electronics Conference and Exposition (APEC), Anaheim, CA, USA, 17–21 March 2019; pp. 521–526. [CrossRef]

31. Reimers, J.; Dorn-Gomba, L.; Mak, C.; Emadi, A. Automotive Traction Inverters: Current Status and Future Trends. *IEEE Trans. Veh. Technol.* **2019**, *68*, 3337–3350. [CrossRef]

32. Poorfakhraei, A.; Narimani, M.; Emadi, A. A Review of Multilevel Inverter Topologies in Electric Vehicles: Current Status and Future Trends. *IEEE Open J. Power Electron.* **2021**, *2*, 155–170. [CrossRef]

33. Kitazawa, O.; Kikuchi, T.; Nakashima, M.; Tomita, Y.; Kosugi, H.; Kaneko, T. Development of Power Control Unit for Compact-Class Vehicle. *SAE Int. J. Altern. Powertrains* **2016**, *5*, 278–285. [CrossRef]

34. Drobnik, J.; Jain, P. Electric and Hybrid Vehicle Power Electronics Efficiency, Testing and Reliability. *World Electr. Veh. J.* **2013**, *6*, 719–730. [CrossRef]

35. Li, W.; Li, G.; Sun, Z.; Wang, Q. Real-time estimation of junction temperature in IGBT inverter with a simple parameterized power loss model. *MIcroelectron. Reliab.* **2021**, *127*, 114409. [CrossRef]

36. Chang, F.; Ilina, O.; Lienkamp, M.; Voss, L. Improving the Overall Efficiency of Automotive Inverters Using a Multilevel Converter Composed of Low Voltage Si MOSFETs. *IEEE Trans. Power Electron.* **2019**, *34*, 3586–3602. [CrossRef]

37. Zhu, J.; Kim, H.; Chen, H.; Erickson, R.; Maksimović, D. High efficiency SiC traction inverter for electric vehicle applications. In Proceedings of the 2018 IEEE Applied Power Electronics Conference and Exposition (APEC), San Antonio, TX, USA, 4–8 March 2018; pp. 1428–1433. [CrossRef]

38. Hecker, Q.; Butrón Ccoa, J.A.; Meyer, W.; Herzog, H.G. Automated design of squirrel-cage induction machines by predefined torque-speed-characteristic. In Proceedings of the 2013 International Electric Machines & Drives Conference, Chicago, IL, USA, 12–15 May 2013; pp. 1160–1165. [CrossRef]

39. Ionel, D.; Eastham, J.; Miller, T.; Demeter, E. Design considerations for PM synchronous motors for flux weakening applications. In Proceedings of the 1997 Eighth International Conference on Electrical Machines and Drives (Conf. Publ. No. 444), Cambridge, UK, 1–3 September 1997; pp. 371–375. [CrossRef]

40. Schätzer, C. Ein Verfahren zur Optimierung bei Elektrischen Maschinen mit Hilfe der Numerischen Feldberechnung. Ph.D. Dissertation, Technische Universität Darmstadt, Darmstadt, Germany, 2001.

41. Robert Bosch GmbH, Green Car Congress. New Bosch 230 Electric Motor and Inverter with Silicon Carbide Technology Offers System Efficiency Up to 97%. 2021. Available online: https://www.greencarcongress.com/2021/09/20210922-bosch.html (accessed on 28 November 2024).

42. Filizadeh, S. *Electric Machines and Drives: Principles, Control, Modeling, and Simulation*; CRC Press: Boca Raton, FL, USA, 2017; p. 237.

43. Igelspacher, J.; Bertram, C.; Flügel, S.; Meyer, W.; Herzog, H.G. Methode für die Auslegung von Asynchronmaschinen in Elektrofahrzeugen. In Proceedings of the Internationaler ETG-Kongress 2013—Energieversorgung auf dem Weg nach 2050, Berlin, Germany, 6 November 2013; p. 7.

44. Lu, C.; Ferrari, S.; Pellegrino, G. Two Design Procedures for PM Synchronous Machines for Electric Powertrains. *IEEE Trans. Transp. Electrif.* **2017**, *3*, 98–107. [CrossRef]

45. Schweigert, D.; Gerlach, M.E.; Hoffmann, A.; Morhard, B.; Tripps, A.; Lohner, T.; Otto, M.; Ponick, B.; Stahl, K. On the Impact of Maximum Speed on the Power Density of Electromechanical Powertrains. *Vehicles* **2020**, *2*, 365–397. [CrossRef]

46. Staton, D.; Chong, E.; Pickering, S.; Boglietti, A. *Cooling of Rotating Electrical Machines: Fundamentals, Modelling, Testing and Design*; IET Energy Engineering Series; Institution of Engineering and Technology: London, UK, 2022; p. 240.

47. Babl, A.; Filusch, D.; Herzog, H.G.; Gerling, D. Development of an Analytical Method for a Driving Cycle-Optimized Design of a Surface-Mounted Permanent Magnet Synchronous Machine. In Proceedings of the 2020 International Conference on Electrical Machines (ICEM), Gothenburg, Sweden, 23–26 August 2020; Volume 1, pp. 124–130. [CrossRef]

48. Murali, N.; Ushakumari, S.; P, M.V. Performance comparison between different rotor configurations of PMSM for EV application. In Proceedings of the 2020 IEEE REGION 10 CONFERENCE (TENCON), Osaka, Japan, 16–19 November 2020; pp. 1334–1339. [CrossRef]

49. Hofmann, W. Maschinelles Lernen als Entwurfshilfe für elektrische Maschinen. *e & i Elektrotechnik und Informationstechnik* **2023**, *140*, 356–365. [CrossRef]

50. Cassimere, B.N.; Sudhoff, S.D. Population-Based Design of Surface-Mounted Permanent-Magnet Synchronous Machines. *IEEE Trans. Energy Convers.* **2009**, *24*, 338–346. [CrossRef]

51. Nicoletti, L.; Köhler, P.; König, A.; Heinrich, M.; Lienkamp, M. Parametric modelling of weight and volume effects in battery electric vehicles, with focus on the gearbox. *Proc. Des. Soc.* **2021**, *1*, 2389–2398. [CrossRef]

52. Gao, B.; Liang, Q.; Xiang, Y.; Guo, L.; Chen, H. Gear ratio optimization and shift control of 2-speed I-AMT in electric vehicle. *Mech. Syst. Signal Process.* **2015**, *50–51*, 615–631. [CrossRef]

53. Kieninger, D.; Hemsen, J.; Köller, S.; Üerlich, R. Automatisierte Auslegung und Optimierung von Getrieben für Elektrofahrzeuge. *MTZ-Mot. Z.* **2019**, *80*, 94–99. [CrossRef]

54. Jurkschat, T.; Lohner, T.; Stahl, K. Improved calculation of load-dependent gear losses by consideration of so far disregarded influences. *Proc. Inst. Mech. Eng. Part J. Eng. Tribol.* **2019**, *233*, 509–519. [CrossRef]

55. Hofstetter, M.; Lechleitner, D.; Hirz, M.; Gintzel, M.; Schmidhofer, A. Multi-objective gearbox design optimization for xEV-axle drives under consideration of package restrictions. *Forsch. Ingenieurwesen* **2018**, *82*, 361–370. [CrossRef]

56. Patil, M.; Ramkumar, P.; Shankar, K. Multi-objective optimization of the two-stage helical gearbox with tribological constraints. *Mech. Mach. Theory* **2019**, *138*, 38–57. [CrossRef]

57. Lu, F.; Cao, X.; Liu, W. Optimal design of high efficiency double helical gear based on dynamics model. *SN Appl. Sci.* **2021**, *3*, 726. [CrossRef]

58. Karadere, G.; Yilmaz, I. Investigation of the Effects of Profile Shift in Helical Gear Mechanisms with Analytical and Numerical Methods. *World J. Mech.* **2018**, *8*. [CrossRef]

59. Paschold, C.; Sedlmair, M.; Lohner, T.; Stahl, K. Calculating component temperatures in gearboxes for transient operation conditions. *Forsch. Ingenieurwesen* **2022**, *86*, 521–534. [CrossRef]

60. Andersson, M.; Sosa, M.; Olofsson, U. Efficiency and temperature of spur gears using spray lubrication compared to dip lubrication. *Proc. Inst. Mech. Eng. Part J. Eng. Tribol.* **2017**, *231*, 1390–1396. [CrossRef]

61. GKN Automotive; Paul Seredynski; SAE International. GKN Demos eTwinster, world's-First 2-Speed Torque-Vectoring BEV Transmission. 2019. Available online: https://www.mobilityengineeringtech.com/component/content/article/44047-sae-ma-03362 (accessed on 28 November 2024).

62. Han, J.O.; Shin, J.W.; Kim, J.C.; Oh, S.H. Design 2-Speed Transmission for Compact Electric Vehicle Using Dual Brake System. *Appl. Sci.* **2019**, *9*, 1793. [CrossRef]

63. Wassiliadis, N.; Steinsträter, M.; Schreiber, M.; Rosner, P.; Nicoletti, L.; Schmid, F.; Ank, M.; Teichert, O.; Wildfeuer, L.; Schneider, J.; et al. Quantifying the state of the art of electric powertrains in battery electric vehicles: Range, efficiency, and lifetime from component to system level of the Volkswagen ID.3. *eTransportation* **2022**, *12*, 100167. [CrossRef]

64. The MathWorks, Inc. *Simulink*; The MathWorks, Inc.: Natick, MA, USA, 2024.

65. Tragfähigkeitsberechnung von Stirnrädern. *Norm DIN 3990-5*; German Institute for Standardization: Berlin, Germany, 1987.

66. *Norm BS EN 10084:1998*; Case Hardening Steels Ð Technical Delivery Conditions. British Standard. British Standards Institution: London, UK, 1998.

67. Shah, R.; Gashi, B.; González-Poggini, S.; Colet-Lagrille, M.; Rosenkranz, A. Recent trends in batteries and lubricants for electric vehicles. *Adv. Mech. Eng.* **2021**, *13*, 16878140211021730. [CrossRef]

68. Graves, S.M. Electric pump system and method. Patent US20190003477A1, 3 January 2019.

69. Deb, K. Multi-objective Optimisation Using Evolutionary Algorithms: An Introduction. In *Multi-Objective Evolutionary Optimisation for Product Design and Manufacturing*; Wang, L., Ng, A.H.C., Deb, K., Eds.; Springer: London, UK, 2011; pp. 3–34. [CrossRef]

70. Behnke, D.; Goddemeier, N.; Möllmer, J.; Wietfeld, C. Comparison of multiobjective optimization algorithms for mobility behaviors in autonomous robot systems. In Proceedings of the 2014 IEEE Globecom Workshops (GC Wkshps), Austin, TX, USA, 8–12 December 2014; pp. 1451–1456. [CrossRef]

71. Nayak, S. Chapter nine—Multiobjective optimization. In *Fundamentals of Optimization Techniques with Algorithms*; Nayak, S., Ed.; Academic Press: Cambridge, MA, USA, 2020; pp. 253–270. [CrossRef]

72. Verma, S.; Pant, M.; Snasel, V. A Comprehensive Review on NSGA-II for Multi-Objective Combinatorial Optimization Problems. *IEEE Access* **2021**, *9*, 57757–57791. [CrossRef]

73. Donoghue, J.F.; Burghart, J.H. Constant Power Acceleration Profiles for Electric Vehicles. *IEEE Trans. Ind. Electron.* **1987**, *IE-34*, 188–191. [CrossRef]

74. Lu, D.; Ouyang, M. Torque-based optimal acceleration control for electric vehicle. *Chin. J. Mech. Eng.* **2014**, *27*, 319–330. [CrossRef]

75. Herrmann, T.; Wischnewski, A.; Hermansdorfer, L.; Betz, J.; Lienkamp, M. Real-Time Adaptive Velocity Optimization for Autonomous Electric Cars at the Limits of Handling. *IEEE Trans. Intell. Veh.* **2021**, *6*, 665–677. [CrossRef]

76. United Nations. Global Technical Regulation on Worldwide Harmonized Light Vehicles Test Procedure. Addendum 15: Global Technical Regulation No. 15 (ECE/TRAN/180/Add.15). 12 March 2014. Available online: https://www.google.com/url?sa=t&source=web&rct=j&opi=89978449&url=https://unece.org/fileadmin/DAM/trans/main/wp29/wp29r-1998agr-rules/ECE-TRANS-180a15e.pdf&ved=2ahUKEwiv9MPiw4aLAxUJVPEDHUghHDYQFnoECCYQAQ&usg=AOvVaw3FxT2bpNeLiUZfEWAutqx_ (accessed on 15 January 2025).

77. Paschold, C.; Sedlmair, M.; Lohner, T.; Stahl, K. Efficiency and heat balance calculation of worm gears. *Forsch. Ingenieurwesen* **2020**, *84*, 115–125. [CrossRef]

78. Doppelbauer, M. *Grundlagen der Elektromobilität*; Springer Vieweg Wiesbaden: Berlin/Heidelberg, Germany, 2020; p. 434. [CrossRef]

79. Arnaudov, K.; Karaivanov, D. *Planetary Gear Trains*; CRC Press: Boca Raton, FL, USA, 2019. [CrossRef]

80. Skolaut, W. *Maschinenbau*; Springer: Berlin/Heidelberg, Germany, 2014; p. 1426.

81. Kirchner, E. *Leistungsübertragung in Fahrzeuggetrieben: Grundlagen der Auslegung, Entwicklung und Validierung von Fahrzeuggetrieben und deren Komponenten*; Springer Vieweg Wiesbaden: Berlin/Heidelberg, Germany, 2007; p. 699. [CrossRef]

82. SKF Group. SKF Rolling Bearings Catalogue. 2023. Available online: https://cdn.skfmediahub.skf.com/api/public/0901d196802809de/pdf_preview_medium/0901d196802809de_pdf_preview_medium.pdf (accessed on 5 December 2024).

83. *Norm ISO 6336-1*; Calculation of Load Capacity of Spur and Helical Gears. International Standard. German Institute for Standardization: Berlin, Germany, 2007.

84. Rosenberger, N.; Rosner, P.; Bilfinger, P.; Schöberl, J.; Teichert, O.; Schneider, J.; Abo Gamra, K.; Allgäuer, C.; Dietermann, B.; Schreiber, M.; et al. Quantifying the State of the Art of Electric Powertrains in Battery Electric Vehicles: Comprehensive Analysis of the Tesla Model 3 on the Vehicle Level. *World Electr. Veh. J.* **2024**, *15*, 268. [CrossRef]

85. Ansys Inc. *Ansys Motor-CAD*; Ansys Inc.: Canonsburg, PA, USA, 2024.

86. Müller, G.; Vogt, K.; Ponick, B. *Berechnung Elektrischer Maschinen*, 6th ed.; Wiley-VCH: Berlin, Germany, 2007.

87. Blaschke, F. The Principle of Field Orientation as Applied to the NEW Transvector Closed-Loop Control System for Rotating-Field Machines. *Siemens Rev.* **1972**, *34*, 217–220.

88. FS820R08A6P2B Datasheet. 2023. Available online: https://www.infineon.com/cms/de/product/power/igbt/automotive-qualified-igbts/automotive-igbt-coolsic-mosfet-modules/fs820r08a6p2b/ (accessed on 3 December 2024).

89. STMicroelectronics. SCTW100N65G2AG Datasheet. 2023. Available online: https://www.st.com/en/power-transistors/sctw100n65g2ag.html (accessed on 3 December 2024).

90. Nguyen, Q.K.; Petrich, M.; Roth-Stielow, J. Implementation of the MTPA and MTPV control with online parameter identification for a high speed IPMSM used as traction drive. In Proceedings of the 2014 International Power Electronics Conference (IPEC-Hiroshima 2014—ECCE ASIA), Hiroshima, Japan, 18–21 May 2014; pp. 318–323. [CrossRef]

91. Donescu, V.; Charette, A.; Yao, Z.; Rajagopalan, V. Modeling and simulation of saturated induction motors in phase quantities. *IEEE Trans. Energy Convers.* **1999**, *14*, 386–393. [CrossRef]

92. Stumberger, B.; Stumberger, G.; Dolinar, D.; Hamler, A.; Trlep, M. Evaluation of saturation and cross-magnetization effects in interior permanent-magnet synchronous motor. *IEEE Trans. Ind. Appl.* **2003**, *39*, 1264–1271. [CrossRef]

93. Nam, K.H. *AC Motor Control and Electrical Vehicle Applications*; CRC Press, Taylor & Francis Group: Abingdon, UK, 2019.

94. Bai, B.; Dezhi, C. Inverter IGBT loss analysis and calculation. In Proceedings of the 2013 IEEE International Conference on Industrial Technology (ICIT), Cape Town, South Africa, 25–28 February 2013; pp. 563–569. [CrossRef]

95. Graovac, D.; Pürschel, M. IGBT Power Losses Calculation Using the Datasheet Parameters, 2009. Available online: https://github.com/stocyr/Projektarbeiten_Semester4/blob/master/Leistungselektronik_Vezzini/Datasheets/04%20-%20IGBT%20Power%20Losses%20Calculation%20Using%20the%20Data-Sheet%20Parameters.pdf (accessed on 3 December 2024).

96. Burkart, R.M.; Kolar, J.W. Comparative Life Cycle Cost Analysis of Si and SiC PV Converter Systems Based on Advanced η-ρ-σ Multiobjective Optimization Techniques. *IEEE Trans. Power Electron.* **2017**, *32*, 4344–4358. [CrossRef]

97. Graovac, D.; Pürschel, M. MOSFET Power Losses Calculation Using the Datasheet Parameters, 2009. Available online: https://github.com/stocyr/Projektarbeiten_Semester4/blob/master/Leistungselektronik_Vezzini/Datasheets/03 MOSFETPowerLossesCalculation.pdf (accessed on 3 December 2024).

98. The MathWorks Inc. *Simscape Battery*; The MathWorks, Inc.: Natick, MA, USA, 2024.

99. European Parliament. Regulation (EU) 2018/858 of the European Parliament and of the Council of 30 May 2018 on the Approval and Market Surveillance of Motor Vehicles and Their Trailers, and of Systems, Components and Separate Technical Units Intended for Such Vehicles, Amending Regulations (EC) No 715/2007 and (EC) No 595/2009 and Repealing DIRECTIVE 2007/46/EC. 2018. Available online: https://eur-lex.europa.eu/eli/reg/2018/858/oj/eng (accessed on 15 October 2021).

100. Humphrey, E.; Elisaus, V.; Rahmani, R.; Mohammadpour, M.; Theodossiades, S.; Morris, N. Diamond like-carbon coatings for electric vehicle transmission efficiency. *Tribol. Int.* **2023**, *189*, 108916. [CrossRef]